UCLA
UCLA Previously Published Works

Title
Experimental study of global-scale turbulence in a librating ellipsoid

Permalink
https://escholarship.org/uc/item/1gf5k6bq

Journal
Physics of Fluids, 26(12)

ISSN
1070-6631

Authors
Grannan, AM
Le Bars, M
Cébron, D
et al.

Publication Date
2014-12-01

DOI
10.1063/1.4903003

Peer reviewed

Experimental study of global-scale turbulence in a librating ellipsoid

A. M. Grannan,[1,a)] M. Le Bars,[1,2] D. Cébron,[3,4] and J. M. Aurnou[1]

[1]*Department of Earth, Planetary, and Space Sciences, University of California, Los Angeles, Los Angeles, California 90095-1567, USA*
[2]*Aix-Marseille Université, CNRS, École Centrale Marseille, IRPHE (UMR 7342), 13384, Marseille Cedex 13, France*
[3]*CNRS, ISTerre, Université Grenoble Alpes, Grenoble, France*
[4]*Institut für Geophysik, ETH Zürich, Sonneggstrasse 5, Zürich CH-8092, Switzerland*

We present laboratory experimental results demonstrating that librational forcing of an ellipsoidal container of water can produce intense motions through the mechanism of a libration driven elliptical instability (LDEI). These libration studies are conducted using an ellipsoidal acrylic container filled with water. A particle image velocimetry method is used to measure the 2D velocity field in the equatorial plane over hundreds libration cycles for a fixed Ekman number, $E = 2 \times 10^{-5}$. In doing so, we recover the libration induced base flow and a time averaged zonal flow. Further, we show that LDEI in non-axisymmetric container geometries is capable of driving both intermittent and saturated turbulent motions in the bulk fluid. Additionally, we measure the growth rate and amplitude of the LDEI induced excited flow in a fully ellipsoidal container at more extreme parameters than previously studied [Noir *et al*., "Experimental study of libration-driven flows in nonaxisymmetric containers," Phys. Earth Planet. Inter. **204-205**, 1 (2012); Cébron *et al*., Phys. Fluids **24**, 061703, "Libration driven elliptical instability," (2012)]. Excitation of bulk filling turbulence by librational forcing provides a mechanism for transferring rotational energy into turbulent fluid motion and thus can play an important role in the thermal evolution, interior dynamics, and magneto-hydrodynamics of librating bodies, as appear to be common in solar system settings [e.g., Comstock and Bills, "A solar system survey of forced librations in longitude," J. Geophys. Res. Planets **108**, 1 (2003)]. © *2014 AIP Publishing LLC.* [http://dx.doi.org/10.1063/1.4903003]

I. INTRODUCTION

The interactions between satellites and their primary gravitational partners distort the shapes of both bodies and give rise to periodic mechanical forcings that, in turn, drive precessional, tidal, and librational motions.[1] The current work focuses specifically on the longitudinal libration in so-called synchronized systems where the secondary body's rotation rate undergoes periodic oscillations about its orbital rate. Additionally, some librating bodies are differentiated and contain liquid metal cores such as those of Mercury,[2] Io,[3] Ganymede,[4] as well as subsurface oceans in Europa,[5] Ganymede,[4] and Enceladus.[6] The fluid layer response to the librational forcing through viscous,[7–9] topographic,[10,11] and electromagnetic coupling[12–14] is important for understanding the thermal, magnetic, and orbital evolution of the body. Importantly, while it is often assumed that thermo-compositional convection drives the fluid motions responsible for dynamo generation,[15–17] recent studies[18–21] have characterized how mechanical forcing can also drive dynamos by injecting a portion of the vast quantity of rotational energy from primary-satellite orbital systems into driving fluid motions.

---

a)Electronic mail: agrannan@ucla.edu

The first studies of libration in spheres[22,23] showed, using pressure measurements, that a resonant response occurs when the forcing frequency matches an eigenfrequency of the system. While this excitation was inferred to be an eigenmode of the system, a recent analytical study in the limit of small viscosity found no resonant excitations and only anomalous pressure variations along the axis of rotation.[24] Librational forcing also gives rise to centrifugal instabilities that are confined to the boundary layers of cylinders and spheres.[7,8] Additional theoretical, numerical, and experimental works have verified the stationary zonal flow caused by non-linear interactions in the Ekman boundary layers of cylinders, spheres, and spherical shells.[8–10,25,26]

Recent studies have focused on simulating librational effects in more realistic geometries that reflect the non-axisymmetric shape of planetary interior fluid layers. Theoretical and numerical studies of flows in non-axisymmetric containers have shown that longitudinal librational forcing cannot, through a *direct* resonance, excite eigenmodes of the system.[27,28] Importantly, this does not preclude the resonance of two inertial modes interacting with an elliptically-deformed base flow.[29,30] Numerical simulations using finite element methods at an Ekman number, $E = 5 \times 10^{-4}$, defined in Sec. II, have shown that a triadic resonance between two inertial modes and a librationally induced elliptically-deformed base flow[31] excites a libration driven elliptical instability (LDEI). This instability gives rise to three-dimensional (3D) motions in the bulk fluid that act to modify the base flow thus truncating the instability. The base flow is then re-established and this cycle of growth and collapse continues.[32] Experimental laser doppler velocimetry (LDV) measurements at a single point attributed a growth and decay of the zonal flow strengths in a half-ellipsoid to the existence of a LDEI.[10] The aspects of the mechanically forced flows, described above, are thoroughly reviewed in Ref. 33.

In this experimental work, a particle image velocimetry (PIV) method is used to measure the libration induced base flow, time-averaged zonal flow, and fully turbulent libration driven flow in the equatorial plane of an ellipsoidal container at a fixed $E = 2 \times 10^{-5}$ more extreme than currently possible through numerical simulations. In Sec. II, the mathematical framework is developed for libration driven flows as well as the resonant conditions and growth rates associated with the LDEI. The experimental method is described in Sec. III and the results are discussed in Sec. IV. The conclusions are presented in Sec. V.

II. MATHEMATICAL BACKGROUND

In this experiment, we consider a homogeneous, incompressible, Newtonian fluid that is enclosed in an ellipsoidal container. The boundary of this shape is specified by the equation for an ellipsoid, $x^2/a^2 + y^2/b^2 + z^2/c^2 = 1$, set in a Cartesian coordinate system affixed to the librating container where $\hat{\mathbf{x}}$ is along the long equatorial axis of the ellipsoid with length a, $\hat{\mathbf{y}}$ is the short equatorial axis with length b, and $\hat{\mathbf{z}}$ is along the axis of rotation with length c. The equatorial ellipticity of the cavity is defined as $\beta = (a^2 - b^2)/(a^2 + b^2)$. The rotation rate $\Omega(t)$ for librational forcing is composed of a constant rotation Ω_0 plus a sinusoidal perturbation

$$\Omega(t) = \Omega_0 + \Delta\varphi\, \omega_{lib} \sin(\omega_{lib} t), \tag{1}$$

where ω_{lib} [rad/s^{-1}] is the angular frequency of libration and $\Delta\varphi$ [rad] is the amplitude of libration. The equations of fluid motion and continuity, written in the librating frame and non-dimensionalized using the long axis a for the length scale and Ω_0^{-1} as the time scale, are

$$\frac{\partial \mathbf{u}}{\partial t} + \mathbf{u} \cdot \nabla \mathbf{u} + 2\big(1 + \epsilon \sin(ft)\big)\hat{\mathbf{z}} \times \mathbf{u} = -\nabla\Pi + E\nabla^2\mathbf{u} - \epsilon f \cos(ft)(\hat{\mathbf{z}} \times \mathbf{r}), \tag{2}$$

$$\nabla \cdot \mathbf{u} = 0. \tag{3}$$

In (2), the first two terms on the left side are the inertial terms, and the third term is the time-dependent Coriolis acceleration. The terms on the right side are the pressure gradient, the viscous dissipation, and the Poincare force due to the time dependent rotation rate, respectively. The non-dimensional libration frequency is $f = \omega_{lib}/\Omega_0$, $\epsilon = f\Delta\varphi$ is the dimensionless libration forcing amplitude, and Π is the modified pressure term containing the time varying centrifugal acceleration. The Ekman number,
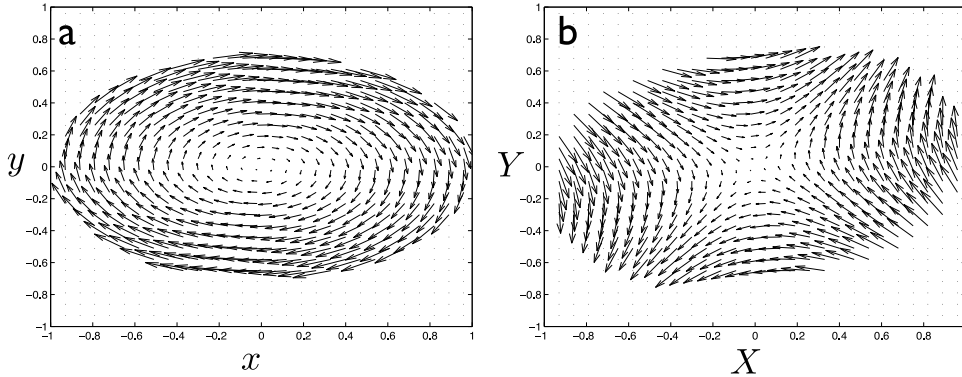
FIG. 1. (a) Theoretical vector field snapshot (U_{lib}, V_{lib}) of the elliptically deformed base flow in the librating frame, (x, y, z). (b) The same base flow transformed into the steadily rotating reference frame, (X, Y, Z), where the current experimental measurements are performed.

$E = \nu/(\Omega_0 a^2)$, characterizes the ratio of viscous to Coriolis forces and $\mathbf{r} = (x, y, z)$ is the position vector in the librating frame.

A. Base flow

Making a perturbation expansion of (2), the flow is decomposed into $\mathbf{u} = \mathbf{U} + \mathbf{u}'$ and $\Pi = \Pi_0 + \pi'$ where the perturbed flow $\mathbf{u}'(\pi')$ is much smaller than the base flow $\mathbf{U}(\Pi_0)$, i.e., $|\mathbf{u}'| \ll \mathbf{U}$ and $\pi' \ll \Pi_0$. Focusing first on the base flow and taking (2) in the limit that $E \ll 1$, the flow is decomposed into $\mathbf{U} = \mathbf{U}_{lib} + \widetilde{\mathbf{U}}$ with an inviscid bulk component, $\mathbf{U}_{lib}$, and a flow in the viscous boundary layer of depth $\sqrt{E}$ attached to the outer boundary, $|\widetilde{\mathbf{U}}| \propto \epsilon$, that is proportional to the libration forcing. An inviscid solution of (2) for the bulk base flow velocity that satisfies the non-penetration condition in the librating frame of reference is given by[29]

$$\mathbf{U}_{lib} = -\epsilon \sin(ft)[\hat{\mathbf{z}} \times \mathbf{r} - \beta \nabla(xy)], \tag{4}$$

with coordinates (x, y, z) and equatorial flow components (U_{lib}, V_{lib}). In the librating frame, fluid parcels oscillate back and forth along elliptically deformed streamlines as shown in a vector field snapshot of Figure 1(a). For the current analysis, this flow is transformed to the steadily rotating frame of reference reflecting the same frame where experimental measurements are performed. This base flow (U_{rot}, V_{rot}) in the steadily rotating frame is given in (5) with X and Y being the spatial coordinates fixed to this frame such that X is aligned with the average location of the container's long-axis. Figure 1(b) shows a snapshot of the oscillating velocity field exhibiting a strain field with an azimuthal wavenumber $m = 2$, and an oscillating direction and amplitude

$$U_{rot} = \epsilon\beta \sin(ft)\Big[Y \cos\left(\frac{2\epsilon(1 - \cos(ft))}{f}\right) - X \sin\left(\frac{2\epsilon(1 - \cos(ft))}{f}\right)\Big]\hat{\mathbf{i}},$$

$$V_{rot} = \epsilon\beta \sin(ft)\Big[Y \sin\left(\frac{2\epsilon(1 - \cos(ft))}{f}\right) + X \cos\left(\frac{2\epsilon(1 - \cos(ft))}{f}\right)\Big]\hat{\mathbf{j}}. \tag{5}$$

B. Zonal flow

In the librating frame, to satisfy the no-slip boundary conditions, viscous corrections in the Ekman boundary layer generate a flow, $\widetilde{\mathbf{U}}$, with axisymmetric and non-axisymmetric components, $\widetilde{\mathbf{U_0}}$ and $\widetilde{\mathbf{U_2}}$, respectively, given as

$$\widetilde{\mathbf{U}} \propto \epsilon \sin(ft)(\widetilde{\mathbf{U_0}} + \beta\widetilde{\mathbf{U_2}}e^{\pm 2i\phi}), \tag{6}$$

where ϕ is the azimuthal angle measured with respect to $\widetilde{\mathbf{X}}$. The non-linear self-interaction of (6) leads to an axisymmetric stationary zonal flow in the boundary layer that, by continuity, generates a flow

in the interior fluid, as confirmed in axisymmetric containers.[8,9,25,34–37] This stationary flow scales as ϵ^2 with an azimuthal wavenumber $m = 0$ and is expected in the ellipsoidal container. Additional axisymmetric and non-axisymmetric stationary flows arise due to the ellipsoidal geometry and scale as $\epsilon^2 \beta$ and $\epsilon^2 \beta^2$ with azimuthal wavenumbers $m = 2$ and $m = 0, 4$, respectively.[38]

C. Inertial modes

For rotating fluids in finite volumes, inertial waves reflected at boundaries conserve the angle between the wave vector and the axis of rotation θ. Thus, reflections and waves may, through constructive interference, generate inertial modes of the form $\mathbf{u}'_j \propto e^{i\lambda_j t}\mathbf{\Phi}_j(\mathbf{r})$ that satisfy the linearized inviscid equation motions given by[39]

$$\frac{\partial \mathbf{u}'}{\partial t} + 2\hat{\mathbf{z}} \times \mathbf{u}' = -\nabla \pi'. \tag{7}$$

The jth inertial mode is the solution of (7) such that

$$i\lambda_j \mathbf{\Phi}_j + 2\hat{\mathbf{z}} \times \mathbf{\Phi}_j = -\nabla \pi'_j, \tag{8}$$

where $\mathbf{\Phi}_j \propto e^{im_j\phi}$ with m_j being the azimuthal wavenumber.[40] Additionally, the inertial modes are orthogonal such that $\int \mathbf{\Phi}_k^* \mathbf{\Phi}_j \, dV = \delta_{j,k}$.[39] Analytical solutions of inertial modes exist for the cylinder,[41] cylindrical shell,[42] spheroid,[43] and a polynomial description also exists for the ellipsoids[44] considered in our experiments. Although, not considered here, such analytical descriptions cannot be extended to the more geophysically relevant geometry of spherical shells due to the ill-posed nature of the well-known Poincaré equation for inertial modes with non-penetrating boundary conditions. Numerical studies, in this geometry, have shown that solutions converge to attractors.[45,46]

D. Elliptical instability

The elliptical instability arises due to the growth of perturbations induced by the interaction between a libration induced base flow from (4) and two inertial modes. Despite the open questions regarding the completeness property of inertial modes whereby an arbitrary velocity field may be expanded into a series of inertial modes,[39] the velocity and pressure perturbations are written as a linear combination of inertial modes and later seek to identify the participating inertial modes experimentally. Then, $(\mathbf{u}', \pi') = \sum_j a_j(t)e^{i\lambda_j t}(\mathbf{\Phi}_j, \pi_j)$ where $a_j(t) \ll 1$ is a small time-dependent coefficient and the evolution for the velocity perturbation in (2) is given by

$$\frac{\partial \mathbf{u}'}{\partial t} + \mathbf{U}_{lib} \cdot \nabla \mathbf{u}' + \mathbf{u}' \cdot \nabla \mathbf{U}_{lib} + 2(1 + \epsilon \sin(ft))\hat{\mathbf{z}} \times \mathbf{u}' = -\nabla \pi' + E\nabla^2 \mathbf{u}'. \tag{9}$$

By substituting the solutions for $(\mathbf{u}', \pi')$ into (9) and analyzing the resulting equations, we seek to determine the conditions that are required on the coefficients a_j such that they grow through time.

$$\sum_j e^{i\lambda_j t}\left\{ \frac{\partial a_j}{\partial t}\mathbf{\Phi}_j + a_j\big[\mathbf{U}_{lib} \cdot \nabla \mathbf{\Phi}_j + \mathbf{\Phi}_j \cdot \nabla \mathbf{U}_{lib} + 2\epsilon \sin(ft)(\hat{\mathbf{z}} \times \mathbf{\Phi}_j)\big] \right.$$
$$\left. + a_j\big(i\lambda_j\mathbf{\Phi}_j + 2\hat{\mathbf{z}} \times \mathbf{\Phi}_j = -\nabla \pi_j\big)\right\}. \tag{10}$$

Here, we have neglected viscous dissipation for simplicity. The last expression in parentheses of (10) is zero using (8). To isolate $\frac{\partial a_j}{\partial t}$, (10) is multiplied by an inertial mode $\mathbf{u}_k'^* \propto e^{-i\lambda_k t}\mathbf{\Phi}_k^*$ and integrated over the entire fluid volume. Using the orthogonality of inertial modes, the evolution of the coefficient a_k is

$$\frac{\partial a_k}{\partial t} = -\sum_j a_j e^{i(\lambda_j - \lambda_k)t} \int \mathbf{\Phi}_k^*\big(\mathbf{U}_{lib} \cdot \nabla \mathbf{\Phi}_j + \mathbf{\Phi}_j \cdot \nabla \mathbf{U}_{lib} + 2\epsilon \sin(ft)(\hat{\mathbf{z}} \times \mathbf{\Phi}_j)\big)dV. \tag{11}$$

The libration driven non-axisymmetric base flow at frequency f with an azimuthal wavenumber $m_{lib} = 2$ may be written as $\mathbf{U}_{lib} \propto e^{\pm i(m_{lib}\phi + ft)}\widetilde{\mathbf{U}_{lib}}(r, z)$ and the inertial mode as $\mathbf{\Phi}_j \propto e^{im_j\phi}\widetilde{\mathbf{\Phi}}_j(r, z)$.

Substituting these dependencies into (11) gives for a_k

$$\frac{\partial a_k}{\partial t} \propto \sum_j a_j e^{i(\lambda_j - \lambda_k \pm f)t} \int e^{i(m_j - m_k \pm m_{lib})\phi} (\widetilde{\mathbf{U}_{lib}} \cdot \nabla \widetilde{\mathbf{\Phi}_j} + \widetilde{\mathbf{\Phi}_j} \cdot \nabla \widetilde{\mathbf{U}_{lib}}$$
$$+ 2\epsilon \sin(ft)(\hat{\mathbf{z}} \times \widetilde{\mathbf{\Phi}_j})) \mathrm{dV}, \qquad (12)$$

and for the coefficient a_j

$$\frac{\partial a_j}{\partial t} \propto \sum_k a_k e^{i(\lambda_k - \lambda_j \pm f)t} \int e^{i(m_k - m_j \pm m_{lib})\phi} (\widetilde{\mathbf{U}_{lib}} \cdot \nabla \widetilde{\mathbf{\Phi}_j} + \widetilde{\mathbf{\Phi}_j} \cdot \nabla \widetilde{\mathbf{U}_{lib}}$$
$$+ 2\epsilon \sin(ft)(\hat{\mathbf{z}} \times \widetilde{\mathbf{\Phi}_j})) \mathrm{dV}. \qquad (13)$$

For the growth of a_k and a_j to occur, the periodicity in time is removed by setting $\lambda_j - \lambda_k \pm f = 0$. The integral over the fluid volume is only non-zero for $m_j - m_k \pm m_{lib} = 0$. These resonant conditions are summarized as

$$|m_j - m_k| = m_{lib},$$
$$|\lambda_j - \lambda_k| = f. \qquad (14)$$

Importantly, the coupled equations show that the interaction of one of the inertial modes $\mathbf{u}'_k, (\mathbf{u}'_j)$ with the base flow $\mathbf{U_{lib}}$ reinforces the other inertial mode $\mathbf{u}'_j, (\mathbf{u}'_k)$. To solve for a_k, we can take the time derivative of (12) and plugging in (13) to get a second order temporal equation for a_k that admits exponential solutions.[30,47] An analogous equation can be made for a_j. Since inertial modes exist within a frequency from $[-2, 2]$, the resonance condition in (14) allows for the existence of elliptical instability in flows from $|f| = 0 - 4$.

E. Growth rates

While these conditions on the frequency and azimuthal wavenumber form a portion of the global analysis of the LDEI, a complete analytical description of the inertial modes is still needed for the large β of our present ellipsoidal geometry. One such method characterizes the inertial modes by assuming a polynomial spatial description of space coordinates for the velocity and decomposes the flow field into a set of basis vectors that satisfy the continuity equation and boundary conditions.[19,44,48] While this method may be extended to any polynomial degree n and thus characterize any coupling of inertial modes, the analytical expressions involved quickly become very complex (e.g., see $n_{poly} = 6$ in Ref. 19), especially for small-scale modes.

Instead, local stability analyses are used to derive analytical expressions of the growth rate for the LDEI. The first approach, using a Wentzel-Kramers-Brillouin (WKB)[49] method for $\epsilon, \beta \ll 1$, gives an upper bound for the growth rate by assuming that short wavelength plane wave perturbations characterized by the wave vector $\mathbf{k}$ whose norm $|k| \gg 1$ are advected along streamlines. The inviscid growth rate σ_{inv} is found by solving the inviscid equations of motion to the first order in $\epsilon \beta$

$$\sigma_{inv} = \frac{16 + f_{res}^2}{64} \beta \epsilon, \qquad (15)$$

where f_{res} is a resonant forcing frequency.[30] This method was confirmed in numerical simulations of the LDEI in Ref. 32.

A second local WKB method uses a multiple scale analysis[50] of a multipolar instability for any ϵ in the limit that $\epsilon \beta \ll 1$. The inviscid growth rate solution is then given by

$$\sigma_{inv} = \frac{16 + (jf_{res})^2}{64} |J_{j-1}(n\Delta\varphi) + J_{j+1}(n\Delta\varphi)| \beta \epsilon, \qquad (16)$$

where J_j is the Bessel function of the first kind with integer j and the resonance condition is written as $|\lambda_1 - \lambda_2| = jf$.[47] The degree n of multipolar deformation is taken to be $n = m_{lib} = 2$ for the ellipsoid. This method was confirmed in the multipolar stability analysis in a librating deformed cylinder and sphere in Ref. 47. A general formula of the typical growth rate for each calculation of

σ_{inv} is given for f around the resonant forcing frequency[30]

$$\sigma_{Theory} = \sqrt{\sigma_{inv}^2 - (f_{res} - f)^2} - K\sqrt{E}. \tag{17}$$

The first term on the right hand side is the band of unstable frequencies about f_{res}, and the second term is the viscous dissipation in the Ekman boundary layer scaling as $E^{1/2}$ where K is a viscous dissipation factor typically between 1 and 10.

The goal of our work here is to quantitatively validate all of the theoretical predictions presented above: (1) the existence of the two-dimensional libration induced base flow in Eq. (5), (2) the zonal flow generated by the non-linear self-interaction of the base flow correction in Eq. (6), and (3) the three-dimensional destabilization via LDEI by making velocity measurements in the equatorial plane of a full ellipsoidal container at Ekman, $E = 2 \times 10^{-5}$. Our work complements and extends the three-dimensional numerical simulations of Ref. 32, performed at larger $E = 5 \times 10^{-4}$, and the experimental analysis of Ref. 10 that made point velocity measurements in the half-ellipsoid.

III. METHOD

A. Experimental approach

The experimental setup used in the present work is adapted from the same apparatus used previously in Refs. 7, 10, and 36. Librational forcing is replicated using two motors. The first, motor rotates the turntable and super-structure at a constant angular velocity of $\Omega_0 = 30$ rpm corresponding to $E = 2 \times 10^{-5}$. The second, which is directly coupled to the acrylic cavity, superimposes a sinusoidal oscillation whose parameter range is $[\Delta\phi, f] = [0.05 - 2.5, 0.5 - 9]$. The container used for this experiment is made from two non-axisymmetric hemispheres machined from solid cast acrylic cylinders and polished for optical clarity. The enclosed fluid cavity is ellipsoidal with a long axis $a = 127$ mm and short axes $b = c = 89$ mm. Axis c is aligned with the axis of rotation and the equatorial ellipticity is fixed in all our experiments at $\beta = 0.34$. A summary of experimental parameters are in Table II of Appendix A.

To characterize meridional fluid motions, direct flow visualizations are performed by using a laser light sheet, oriented along a vertical plane that passes through the container's origin, to light Kalliroscope™ particles suspended in the water. A Canon EOS 7D digital camera with a resolution of 1080×720 pixels is positioned on the rotating table to the side of the container to record movies of the meridional flow field at 60 frames per second.

To make quantitative measurements, a PIV technique is employed in the rotating reference frame. Nearly spherical, 100 μm diameter Optimage™ particles of density $(1 \pm 0.02$ g/cm$^3)$ are added to the water. Four laser light sheets are fixed in the librating frame several millimeters above the equatorial plane due to the presence of the joining seam for the two acrylic hemispheres. The camera is fixed in the rotating frame, positioned overhead (i.e., Figure 2), in order to acquire 1080×720 resolution movies of the horizontal flow field. These movies are made only after solid body rotation has been reached; they are initiated at the start of oscillatory motion and the recordings are typically 12 min in duration. The camera is connected directly to a computer in the rotating frame, which, in turn, is controlled remotely from the lab frame.

Additionally, the camera settings were optimized and physical masks were implemented to produce well-resolved movies that could yield accurate PIV results. These movies are separated into their constituent frames and passed through an open source PIV software, DPIVSoft2010,[51] that has been successfully employed in previous studies.[9,52] The velocity field for an entire equatorial plane is resolved into a 23 x 40 grid with a typical spatial resolution of 8 mm. All velocity measurements presented below have been non-dimensionalized using the long axis length, a, and the steady rotational period Ω_0^{-1}.
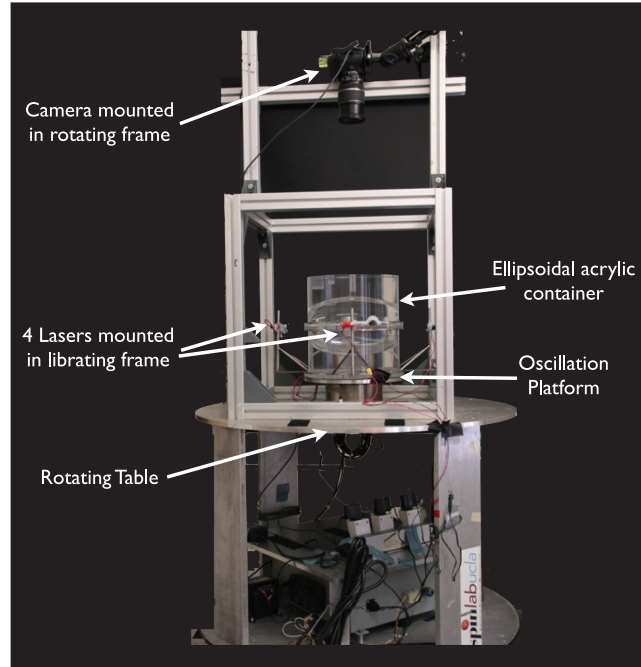
FIG. 2. The libration experimental apparatus. The high definition camera is shown in top view position for PIV. The camera is also used in side-view for Kalliroscope visualizations of meridional flows.

IV. RESULTS

A. Base flow

Figure 3(a) shows an instantaneous PIV vector field of the elliptically deformed base flow in the fluid interior induced by the topographic coupling of the librating non-axisymmetric boundary for $f = 1.46, \epsilon = 0.73$. This comparison provides a qualitative match to the bulk interior inviscid solution of the base flow[29] in the steadily rotating reference frame shown in Figure 1(b). For a quantitative comparison, Figure 3(b) shows a profile of the magnitude of the base flow velocity, $|U|$ (squares), along the X-axis (dashed black line in Figure 3(a)) compared to the theoretical base flow (solid black line) in Figure 3(b) at the same phase of libration. The experimental results in Figure 3(b) follow the base flow trend while the velocity magnitudes are slightly above the
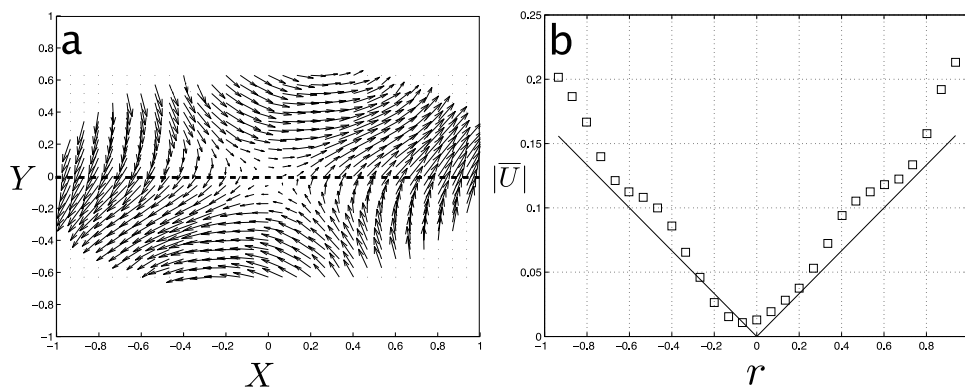

FIG. 3. PIV data for $f = 1.46, \epsilon = 0.73$. (a) Snapshot showing the libration induced base flow and (b) the snapshot profile of the velocity magnitude $|U|$ (squares) along the X-axis (dashed black line in (a) with the theoretical base flow from (5) (black line)).
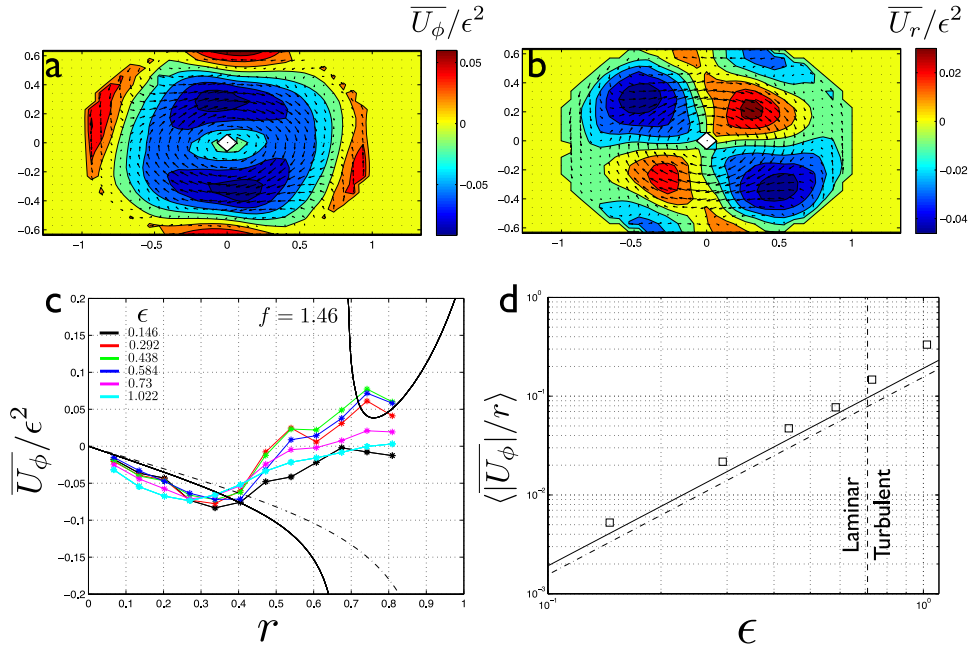
FIG. 4. (a) Zonal flow azimuthal velocity $\overline{U_\phi}/\epsilon^2$ and (b) zonal flow radial velocity component $\overline{U_r}/\epsilon^2$ for ($f = 1.46$; $\epsilon = 0.73$) normalized by ϵ^2. (c) Radial profile of the normalized azimuthal velocity profile $\overline{U_\phi}/\epsilon^2$. (d) Comparison of spatially averaged $\langle|\overline{U_\phi}|/r\rangle$ from $r \in [0.1 \sim 0.35]$ as a function of ϵ with theoretical values $\langle|\overline{U_\phi}|/r\rangle = 0.156\epsilon^2$ from Busse (2010) (dashed black line) and $\langle|\overline{U_\phi}|/r\rangle = 0.192\epsilon^2$ from Sauret and Le Dizes (2013) (solid black line). Experimental results (squares) for $E = 2 \times 10^{-5}$, $f = 1.46$; $\epsilon = 0.146, 0.292, 0.438, 0.584, 0.73$, and 1.022 are provided in Table III of Appendix B.

theoretical flow with an increase near the boundaries. This deviation is associated with the axisymmetric flow generated through viscous non-linear interactions in the boundaries driving a zonal flow.

B. Zonal flow

An analysis of the zonal flow is performed for fixed $f = 1.46$ and $E = 2 \times 10^{-5}$ for six values of ϵ in the range $[0.146 - 1.022]$. We make use of continuous PIV measurements in the equatorial plane averaged over at least 50 libration cycles. Figure 4(a) shows a time-averaged azimuthal velocity $\overline{U_\phi}/\epsilon^2$ contour plot. Since the system rotation is counter-clockwise, a mean zonal flow in the bulk is clockwise (retrograde) in all cases studied. Figure 4(b) clearly shows the $m = 2$ structure in the time-averaged radial velocity $\overline{U_r}/\epsilon^2$ reflecting the $m_{lib} = 2$ ellipsoidal container.

Figure 4(c) shows a linear collapse of the radial profiles of $\overline{U_\phi}$ when normalized by ϵ^2 indicating the presence of the theoretically predicted solid body rotation between $r = [0.1 \sim 0.35]$ whose magnitude scales as ϵ^2. Theoretical zonal flow radial profiles are taken from Ref. 34 (black dotted-dashed line) and from Ref. 26 (solid black line). Both theoretical flows include singularities around the critical cylindrical radius[53] $s_c = \sqrt{1 - f^2/4}$ due to the exclusion of inertial modes for $f \leq 2$. For a spherical geometry, Ref. 34 assumes $f, \epsilon \ll 1$ with $s_c = 1$ while Ref. 26 assumes that $\epsilon \ll 1$ and $s_c = 0.68$ for $f = 1.46$. Inertial modes generate internal shear layers whose affect on the zonal flow is still poorly understood. Thus, solid body zonal flow is expected for $r \ll s_c$ where the profiles are nearly linear and may help explain the deviation of the experimental velocity profiles with the theoretical trends.

The linear collapse of the velocities for all cases studied between $r = [0.1 \sim 0.35]$ is indicative of the presence of the theoretically predicted solid body rotation whose magnitude scales as ϵ^2 such that $|\overline{U_\phi}| = \alpha\epsilon^2 r$ where α is a prefactor. Figure 4(d) shows the average experimental values of the $\langle|\overline{U_\phi}|/r\rangle$ between $r = [0.1 \sim 0.35]$ at each ϵ. The same averaging is performed for the theoretical profiles yielding $\alpha = 0.156$ from Ref. 34 (black dot-dash line) and $\alpha = 0.192$ from Ref. 26 (solid black
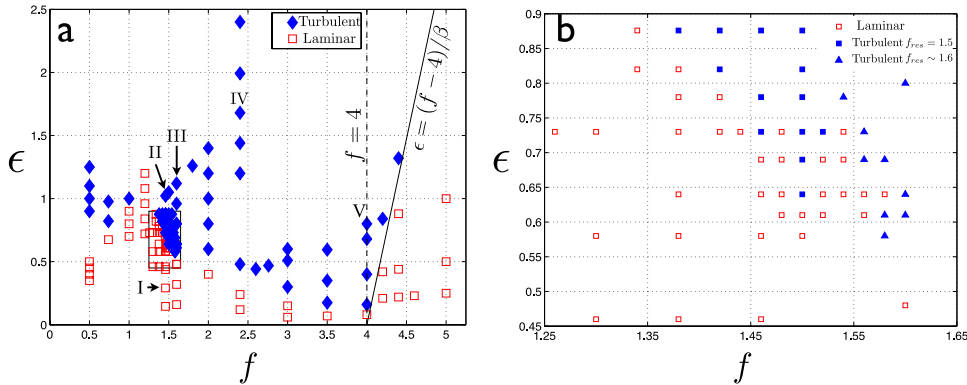
FIG. 5. (a) Laminar (open red squares) where I shows the case $f = 1.46; \epsilon = 0.292$ is used in Figure 6(I). Turbulent cases (blue-filled symbols) are found from $f = 0$ to $f = 4$ (dashed black line) and up to $f = 4 + \epsilon\beta$ (solid black line). The non-dimensional velocity Ro_{eq} and associated Re_{eq} for cases II-V are shown in Figure 6(II-V) while the associated flow structures, shown in Figure 7(II-V), are used for LDEI confirmation. (b) A fine scale diagram of the box where turbulent flows are distinguished by separate coupled modes associated with $f_{res} = 1.5$ (blue squares) and $f_{res} \sim 1.6$ (blue triangles).

line). The experimental values scale with ϵ^2 in good agreement with the theoretical values attained in the spherical geometry despite the rather large ϵ and f, and the finite equatorial ellipticity of the container used in the experiment. The scaling of the minimum flow velocity with ϵ^2 is indicative of the possibility for shear instability as shown for tidal forcing experiments.[54] However, this instability was shown to generate local turbulence and does not explain the bulk interior turbulence observed in our experiments.

The universal quadratic scaling of the axisymmetric component of the zonal flow helps explain the lack of dependence on the geometry found from the LDV measurements in Ref. 10. Those point measurements, on time-average at a fixed radius, remove any non-axisymmetric component. Importantly, this data includes a transition from laminar to turbulent flow, determined through side view-visualizations, that will be discussed in the Sec. IV C. This transition occurs around $f = 1.46$; $\epsilon = 0.71$ (vertical dashed line in Figure 4(d)).

C. LDEI

1. Libration regime diagram

By varying $f \in [0 - 9]$ and maximizing the range of ϵ for each f, a regime diagram of laminar (red open squares) and turbulent flows (closed blue diamonds) in the $[f, \epsilon]$ parameter space is constructed in Figure 5(a). Note that we focus on the range $f \in [0 - 5]$ in Figure 5(a) since no turbulent flows were found in the range $f \in [5 - 9]$. The rectangle in the regime diagram is magnified in Figure 5(b) where, by fine variations in $[f, \epsilon]$ space, two separate turbulent cases are distinguished as well the threshold of stability. The verification of the LDEI is performed using cases $f = 1.46, 1.5, 1.6, 2.4, 4$ with $\epsilon = 1.022, 1.05, 1.12, 1.68, 0.8$, respectively. The experimental data from Fig. 5 is provided in Appendix B: Table IV.

As the librational forcing frequency f and strength ϵ are varied, the libration driven flows are separated by side-view direct visualization into laminar and turbulent flows. From equatorial PIV analysis, measurements of the spatially averaged magnitude of the velocity are non-dimensionalized using the long axis length a and steady rotational period Ω_0^{-1}. Thus, we define an equatorial Rossby number, $Ro_{eq} = \langle |U| \rangle$, as the ratio of inertial to Coriolis forces. Additionally, for fixed $E = 2 \times 10^{-5}$, an equatorial Reynolds number, $Re_{eq} = Ro_{eq}/E$, provides a measure of equatorial flow turbulence.

A comparison of laminar and turbulent flows are shown in Figure 6 with Ro_{eq} on the left axis and associated Re_{eq} on the right axis using four measurements per libration cycle filtered over a moving window average over 10 librational periods with a 90% overlap. In side-view, laminar flows exhibit calm flow in the bulk interior and do not exhibit any vertical motions. Figure 6(I) shows the steady flow at $f = 1.46$; $\epsilon = 0.292$ with no clear growth phase.
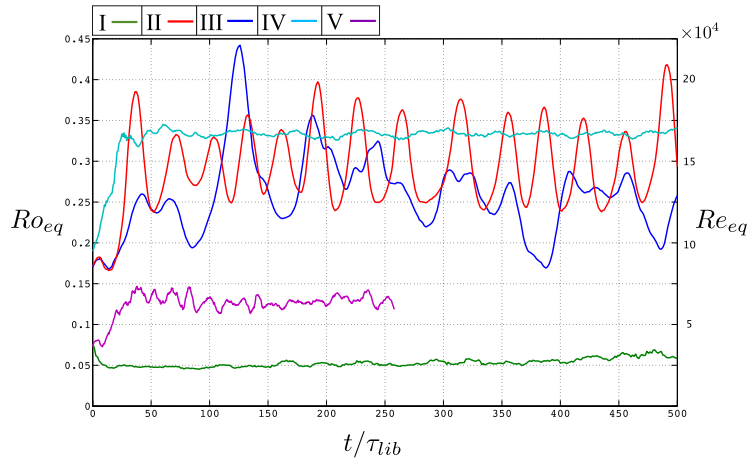
FIG. 6. Time evolution of the non-dimensional spatially averaged velocity $Ro_{eq} = \langle |U| \rangle$ and associated $Re_{eq} = Ro_{eq}/E$ using four points per libration cycle over 500 librational periods where $\tau_{lib} = 2\pi/\omega_{lib}$. The data is filtered using a moving average window over 10 libration cycles with a 90% overlap. I. The laminar case ($f = 1.46; \epsilon = 0.292$). The intermittently turbulent flows of II. ($f = 1.46; \epsilon = 1.022$) and III. ($f = 1.6; \epsilon = 1.12$), and saturated turbulent flows of IV. ($f = 2.4; \epsilon = 1.68$) and V. ($f = 4; \epsilon = 0.8$).

Turbulent flows exhibit three-dimensional motions with either intermittent or saturated turbulence in the bulk interior. First, intermittently turbulent flows, as seen in side-view and from studies Refs. 10 and 32, are characterized by the growth of the LDEI until the flow collapses after some time, leading to relaminarization and the re-establishment of the base flow and, by extension, the LDEI itself becomes cyclic. Figure 6(II) and 6(III) show the intermittent turbulence in cases $f = 1.46; \epsilon = 1.022$ and $f = 1.6; \epsilon = 1.12$. After an initial growth phase, the intermittently turbulent cases show large cycles of growth and collapse. For these two cases $\overline{Ro_{eq}}$ = [0.249, 0.299] with variances [$2.3 \times 10^{-3}, 2.6 \times 10^{-3}$]. The strength of the resulting turbulence is $\overline{Re_{eq}}$ = [$1.2 \times 10^4, 1.4 \times 10^4$] $\gg 1$ emphasizing the strong turbulence generated.

Figure 6(IV) and 6(V) show the saturated turbulence in cases $f = 2.4; \epsilon = 1.68$, and $f = 4; \epsilon = 0.8$. For these cases, after an initial growth phase, the cycles are smaller than for intermittent turbulence and side-view visualizations show that once the bulk turbulence is initiated, no clear cycles are visible. As such, the corresponding variances in these cases are an order of magnitude smaller [$3.05 \times 10^{-4}, 1.88 \times 10^{-4}$] while the strong turbulence persists with $\overline{Re_{eq}}$ = [$1.65 \times 10^4, 6.25 \times 10^3$] $\gg 1$. However, a comparison of intermittent and saturated turbulent flows in Figures 6(III) and 6(V) shows the existence of qualitatively similar cycles above the base state despite the clear distinction in side-view visualization discussed. A more quantitative distinction between flows as well as the long term turbulent evolution will be the subject of future studies. Values for $\overline{Ro_{eq}}$ and the variance for each case studied are given in Appendix B: Table III.

The existence of these turbulent flows span from $f = 0$ to $f = 4$ (dashed vertical line in Figure 5(a)) in agreement with the range provided by the resonant conditions, (14), for the LDEI. Specifically, even if a direct resonant forcing was to exist, there can be no direct forcing mechanism causing excitations in the range $f \in [2 - 4]$. As f is increased, the growth rate increases following the WKB formulation of (17) and thus the stability threshold separating laminar and turbulent flows decreases to a minimum at $f = 4$. Figure 5(b) shows a finer scan of the stability threshold around $f = 1.46$ with an intermingling of laminar and turbulent flows. By comparing the symmetry of the excited flow at $f = 1.46$, discussed further in the Sec. IV C 2, we distinguish separate symmetry properties from the LDEI of other cases around $f_{res} \sim 1.6$ and track the excited LDEI for $f = 1.46$ to a minimum at $f = 1.5$. Since the growth rate in (17) attains a maximum when $f = f_{res}$, the associated stability threshold also attains a local minimum. Thus, we find that the LDEI associated with $f = 1.46$ has its source at $f_{res} = 1.5$. As a consequence of the rather large Ekman number used in our experiment, only selected resonances can occur and, as the Ekman number is reduced, more
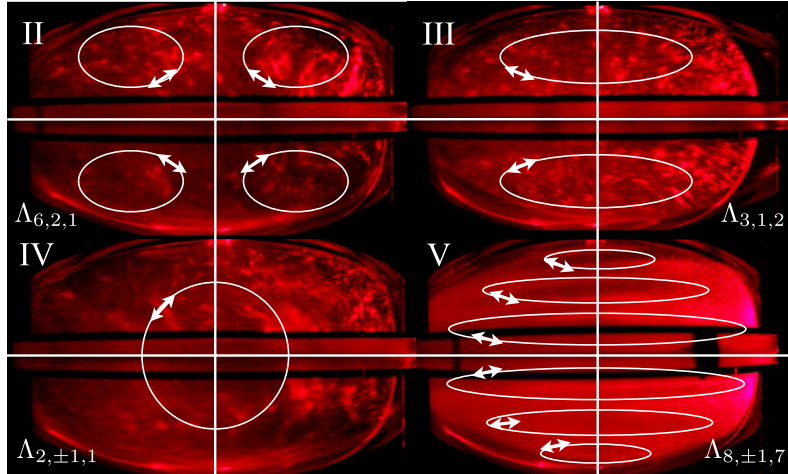
FIG. 7. Direct side-view visualization snapshots of the turbulent flow cases indicated in Figure 5(a) and Figure 6(II-V) with II. ($f = 1.46, 1.5; \epsilon = 1.022, 1.05$) III. ($f = 1.6; \epsilon = 1.12$), IV. ($f = 2.4; \epsilon = 1.68$), and V. ($f = 4; \epsilon = 0.8$). Representative inertial modes, $\Lambda_{n,m,k}$ are taken from polar flattened spheroid calculations in Ref. 56. Movies for these individual cases are available as a supplement to this work online. (Multimedia view) [URL for II: http://dx.doi.org/10.1063/1.4903003.1] [URL for III: http://dx.doi.org/10.1063/1.4903003.2] [URL for IV: http://dx.doi.org/10.1063/1.4903003.3] [URL for V: http://dx.doi.org/10.1063/1.4903003.4]

resonances may be excited leading to transition from the intermingling of laminar and turbulent states to a sharper boundary between the two as seen in studies of tidal instability in Ref. 55.

Furthermore, excitations beyond $f = 4$ are associated with a higher order solutions in $\epsilon\beta$ at the large ellipticity β of the container and the large librational forcing ϵ.[49] The large ϵ and β limit of instability is $f = 4 + \epsilon\beta + O(\epsilon^2\beta^2)$ and the black line associated with the limit is shown in Figure 5(a) as $\epsilon = (f - 4)/\beta$ and is confirmed by the data. Additionally, the existence of many novel turbulent flows including $f = 1, \epsilon = 1$, builds upon the previous experimental work in the half-ellipsoid of Ref. 10 that prevented the growth of turbulent flows via elliptical instability of equatorially antisymmetric inertial modes.

2. Mode coupling

Here, we seek to demonstrate that the presence of bulk turbulent flow in our system is due to the LDEI, i.e., to the resonance of two inertial modes with a libration induced base flow. To do so, we combine several techniques including the identification of the inertial modes from side-view direct visualizations using Kalliroscope, and via Fourier analysis of filtered reconstructions of the velocity fields and growth rate measurements from the equatorial plane PIV data. Figure 7 (Multimedia view) shows snapshots from side-view movies for four of the distinct modes observed during the amplitude growth of the inertial mode. [Movies for these cases are available in the caption to Fig. 7 as a supplement online] We use spheroidal inviscid modes, $\Lambda_{n,m,k}$, from Ref. 56 to both look for modes with similar flow structures and symmetries and find the simplest mode couplings. Here, n is the degree of the associated Legendre polynomial that combines the radial and axial wavenumbers, m is the azimuthal wavenumber for the mode, and k represents the kth eigenfrequency. The general schematic for the dominant modes with the largest frequency is superimposed in white on Figure 7.

The clearest determination of the mode and frequency coupling is provided using the $f = 4$ case at the extreme range of the instability where we expect the participating modes with eigenfrequencies $|\lambda_{1,2}| = f/2 = 2$. First, the side-view visualization in Figure 7(V) shows a large number of structures stacked horizontally as might be expected from the inertial wave dispersion relation for $|\lambda_{1,2}| = 2$ where the wave vector is parallel to the rotation axis. Second, Figure 8 shows the power spectrum of the velocity magnitude for $f = 4$ where the strongest peaks are associated with the librational forcing frequency at $f = 4$, steady zonal flow around $f = 0$, and the inertial modes
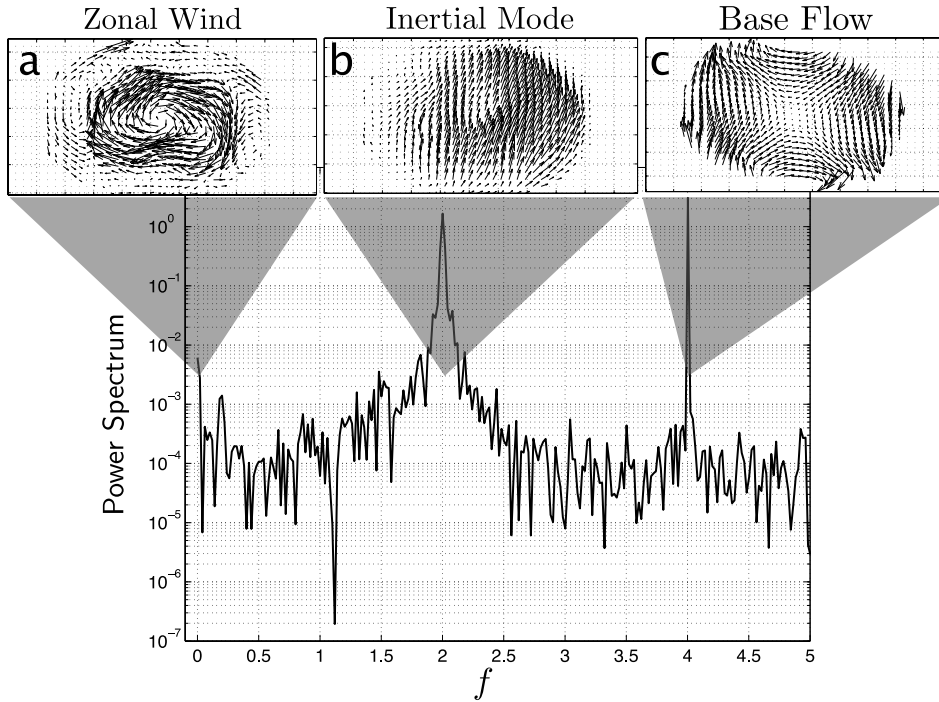
FIG. 8. Power spectrum of the velocity magnitude for $f = 4$; $\epsilon = 0.8$. (a) Steady component with snapshot of filtered steady component of flow. (b) Snapshot of the filtered $m_{1,2} = |1|$ inertial mode at half the driving frequency $\lambda_{1,2} = |f/2|$ satisfying the resonance conditions. (c) The filtered snapshot of the librational base flow at the driving frequency f.

at $|\lambda_{1,2}| = f/2$. The filtered reconstruction at this frequency shows that the base flow in Figure 8(c) is in good qualitative agreement with the libration driven base flow of Figure 1(b). A retrograde zonal flow snapshot is reconstructed around the zonal wind frequency, $f = 0$, in Figure 8(a). Finally, the flow in Figure 8(b), filtered around $f = 2$, is identified as an $|m| = 1$ inertial mode and the side view helps us identify the spherical modes $\Lambda_{8,1,7}$ and $\Lambda_{8,-1,7}$ that exhibit a similarly large vertical wavenumber and $|m| = 1$ near the equator.

For the LDEI in the $f = 1.46, 1.5, 1.6, 2.4$ cases, such a complete confirmation of the resonance conditions is more complicated for several reasons. Figure 9(a) shows the temporal fast Fourier transform (FFT) for the case of $f = 1.5$ where two distinct inertial mode frequencies are found only by carefully choosing the area of the PIV field to perform the FFT. These distinct frequencies are found around $\lambda_1 \sim 1.62$ close to the driving frequency f and the second inertial mode with
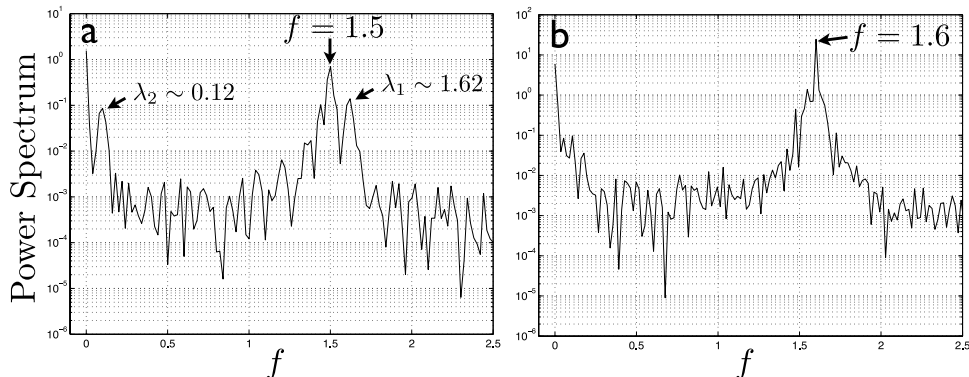

FIG. 9. Power spectrum of the velocity magnitude for (a) $f = 1.5$; $\epsilon = 1.05$ and (b) $f = 1.6$; $\epsilon = 1.12$ showing the most prominent peaks at the forcing frequency f and for the steady component $f = 0$.
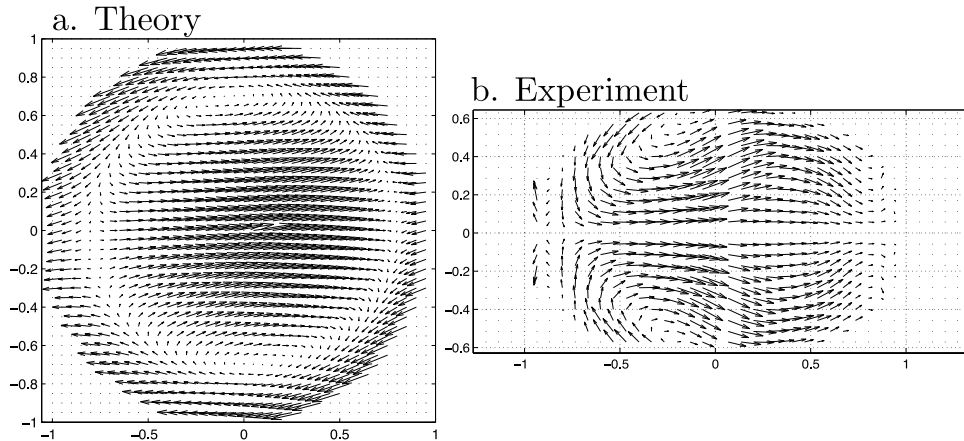
FIG. 10. Comparison of snapshots for (a) the equatorial plane of the theoretical spherical inviscid mode $\Lambda_{3,1,2}$ and (b) the filtered reconstruction of the experimental equatorial flow around the driving frequency with the even $m = 2$ symmetry removed for ($f = 1.6$, $\epsilon = 1.12$).

frequency $\lambda_2 \sim 0.12$ close to the zonal wind frequency. Figure 7(II) shows that the mode excited around $f = 1.46$ and $f = 1.5$ is symmetric across both the equator and the meridional axis. The dominant excited flow structures, as seen from the vertical cross-section, are qualitatively similar to the mode $\Lambda_{6,2,1}$ with the frequency closer to the driving frequency and azimuthal wavenumber $m = 2$. A second possible mode, coupled to form the LDEI, is similar to the inertial mode, $\Lambda_{8,4,2}$, with a frequency close to zero with $m = 4$. This low frequency mode is not clear in the Kalliroscope movies that only show strong shear structures. Filtered flow reconstruction around the driving frequency cannot distinguish an $m = 2$ or $m = 4$ mode because of its superimposition with the base flow driven by the $m = 2$ librational forcing. At the low frequency, an inertial mode cannot be clearly distinguished from the zonal flow. However, further arguments in favor of the LDEI triadic resonance in this case will be given below using the growth rate calculations.

For the $f = 1.6$ case, analysis of the FFT spectrum in Figure 9(b) does not yield any additional peak aside from the zonal flow and forcing frequency. The side-view visualization in Figure 7(III) shows that the coupled modes are symmetric across the equator and anti-symmetric across the meridian. This description is similar to $m = 1$ inviscid modes $\Lambda_{3,1,2}$ near the forcing frequency and the possible coupling of the $m = 3$ mode, $\Lambda_{5,3,1}$, closer to zero. Since the librational forcing, $m = 2$, is even and the proposed mode coupling is odd, the even symmetry is subtracted around the forcing frequency indeed revealing an m = 1 mode as shown in Figure 10. Figure 10(a) shows the theoretical spheroidal mode $\Lambda_{3,1,2}$ while Figure 10(b) shows the subtraction of the even symmetry around $f = 1.6$ in the PIV data revealing a separate odd symmetry associated with the excited inertial mode. The similarity between the two images provides a qualitative verification for $m = 1$ inertial mode near the driving frequency. No additional low frequency mode can be distinguished from the steady zonal flow.

Finally, side-view visualizations indicate that the triadic resonance at $f = 2.4$ are due to a coupling of spinover modes. Each mode is characterized by rotation about an axis perpendicular to the rotation axis as indicated in Figure 7(IV). Because the velocity at the equator is dominated by vertical motion, the PIV data taken of the horizontal velocity does not provide a clear insight into the excited spinover mode coupling. The spinover inviscid mode descriptions $\Lambda_{2,1,1}$ and $\Lambda_{2,-1,1}$ provide a qualitative analytical structural comparison with Figure 7(III), while a polynomial decomposition of the spinover mode in Ref. 44 gives the inviscid inertial mode frequencies at $|\lambda_{1,2}| = 1.15$, yielding $f_{res} = 2.3$. This value is close to the observed frequency $f = 2.4$.

In general, we find that the coupling of a mode near the libration forcing frequency with a low frequency mode is always associated with the intermittent turbulence whose velocity magnitude is shown in Figure 6(II) and 6(III) while the coupling of inertial modes with frequencies $\pm f/2$, including the spinover mode coupling, is associated with saturated turbulence from Figure 6(IV)

TABLE I. Growth rates for the LDEI in $f = 1.46, 1.5, 1.6$; $\epsilon = 1.022, 1.05, 1.12$ taking f_{res} and ϵ_{Thresh} from the regime diagram in Figure 5(b). σ_{Data} is extracted from a fit of the spatially averaged magnitude of velocity $\langle |U| \rangle$ filtered through a moving window average over 10 libration cycles with an overlap of 90%. (a) The comparison with the WKB stability analysis from (15). (b) The comparison with the asymptotic multipolar stability analysis from (16).

f	ϵ	f_{res}	ϵ_{Thresh}	$K_{Thresh}(a)$	$\frac{\sigma_{Theory}}{\sigma_{Data}}(a)$	$K_{Thresh}(b)$	$\frac{\sigma_{Theory}}{\sigma_{Data}}(b)$
1.46	0.876	1.5	0.69-0.73	12.0-13.1	0.95-1.2	7.3-9.2	0.59-1.2
1.46	1.022	1.5	0.69-0.73	12-13.1	0.65-1.3	7.1-7.8	0.83-1.1
1.5	1.05	1.5	0.61-0.64	13.2-13.9	0.95-1.2	8.3-9.9	0.74-0.96
1.6	1.12	1.6	0.48-0.61	10.9-13.5	0.71-1.0	3.4-5.1	0.55-0.78

and 6(V). Furthermore, the coupling of large scale inertial modes for $f = 1.46$ and $f = 1.6$ are promoted by the large Ekman number in our experiment. As the Ekman number is decreased toward planetary values, more resonance couplings excite smaller scale modes that are the most unstable through the WKB analysis of the growth rates.[55,57] In this sense, the small scale inertial modes with frequencies $\pm f/2$ excited by $f = 4$ case may be more relevant to planetary applications.

3. Growth rates

To verify the LDEI growth rate, we focus on the $f = 1.46, 1.5$ and $f = 1.6$ cases where the excited modes have non-zero horizontal velocities and the Fourier analysis is unconvincing. The regime diagram in Figure 5 provides upper and lower bounds for the stability threshold at each f. A fine regime diagram of the boxed-in area is shown in Figure 5(b). Using side-view visualizations, the laminar and the separated turbulent cases associated with $f = 1.46, 1.5$ and $f = 1.6$ can be distinguished. Finding the threshold in the fine regime diagram at $f = 1.5$ verifies that the resonant frequency associated with the $f = 1.46, 1.5$ is $f_{res} = 1.5$ around $\epsilon_{thresh} \in [0.61 - 0.64]$ and $\epsilon_{thresh} \in [0.69 - 0.73]$ for $f = 1.46$. The threshold around the resonant frequency for $f = f_{res} = 1.6$ is $\epsilon_{thresh} \in [0.48 - 0.61]$.

At the threshold of instability where $\sigma = 0$, by using $\sigma_{inv}(f_{res}, \epsilon_{thresh})$ in (15), we solve for the dissipation factor K to get a range for $K_{thresh} = K$. By plugging this range into (17), a range of values for σ_{theory} is created. Separately, σ_{Data} is calculated after filtering spatially averaged PIV velocity magnitude of four points for every libration cycle using running average over 10 libration cycles with a 90% overlap. To compare the theoretical growth rate with the data, the growth phase is fitted to an equation of the form $\langle |U| \rangle = A + B e^{\sigma_{Data}(t-t_0)}$ where A and B are fitting coefficients.

Table I shows the value range $\sigma_{Theory}/\sigma_{Data}$ and its range for $f = 1.46, 1.5, 1.6$ using (a) a local WKB analysis using plane wave perturbations of (15) and (b) a separate multiple scale asymptotic WKB analysis using (16). This finds good agreement between the theoretical growth rates using the local approaches and the measured growth rates for $f = 1.46$, $f = 1.5$, and $f = 1.6$ where for perfect agreement $\sigma_{Theory}/\sigma_{Data} = 1$ despite discrepancies that result since neither $\epsilon \ll 1$ nor $\epsilon\beta \ll 1$ holds at the large experiments values used. The error associated with the growth rate ratios stems from the noise from PIV signal in measuring σ_{Data} and in the determination of ϵ_{thresh} using Figure 5(b) that is used to deduce K_{thresh}.

V. DISCUSSION AND CONCLUDING REMARKS

In the present experimental study, we have used a combination of direct flow visualizations and PIV measurements in the equatorial plane to prove the existence of the libration driven elliptical instability, LDEI, as the cause of intermittent and saturated space filling turbulence in the interiors of an ellipsoidal container. To do so, we have explored the flow regimes found in longitudinal libration in the (f,ϵ)-parameter space at a fixed Ekman number $E = 2 \times 10^{-5}$. Our results confirm that the librationally induced base flow is established in the bulk and is in good quantitative agreement with the theoretical base flow when transformed into the steadily rotating frame. We have been able to quantitatively distinguish between laminar flows and intermittent or saturated turbulent flows in

the bulk interior. By analyzing the zonal flow induced by the non-linear interaction of the librational forcing, we recover a $|U_\phi| \sim \epsilon^2$ scaling behavior. We have found the presence of turbulent fluid motions from $f \in [0 - 4]$ in accordance with the theoretical limits of the resonance condition for the LDEI. By choosing the most representative examples of the turbulent flows, we have used the $f = 4$ case to verify the spatial and temporal resonance conditions and the $f = 1.46, 1.5, 1.6$ to verify the theoretical growth rate calculations.

While we have identified the essential characteristics of LDEI, several important questions remain. The first open question is the origin of the difference between the onset of intermittent and saturated turbulence. The analysis indicates that intermittently turbulent flows are generated through a LDEI having inertial modes near driving frequency, f and at a low frequency inertial mode that may be obscured by the zonal flow. For cases where saturated turbulence persists, the participating inertial modes have frequencies at $\pm f/2$. Secondly, due to current experimental difficulties, we have only measured the velocity in the nearly equatorial plane and, thus, it is not possible to fully measure the energy associated with turbulent three-dimensional motion.

Although our experimental parameters are far from planetary values, we have confirmed the characteristics of the LDEI mechanism by compensating for large Ekman number with the exaggerated equatorial ellipticity of our experimental container. As such, we may extrapolate from our current work to planetary settings using the growth rate formula (17) and planetary values to provide a critical value for the equatorial ellipticity needed to generate a planetary LDEI following Ref. 32. By requiring a positive growth rate and assuming perfect resonance $f = f_{res}$, (17) is rewritten as $\beta_c > 64K\sqrt{E}/(16 + f_{res}^2)\epsilon$. Using parameters for longitudinal libration where $f = 1$, $E \sim 10^{-14}$, $\epsilon \sim 10^{-4}$ and a minimum dissipation factor $K = 1$, the critical ellipticity is $\beta_c > 10^{-3}$ indicating that Io, Europa, and telluric exoplanets CoRoT-7b, GJ1214b, and 55CnCe can support turbulent interior fluid motions generated by LDEI.[30]

Furthermore, we find a lower bound on the amount of rotational energy injected into the fluid layer through equatorial plane measurements at $E = 2 \times 10^{-5}$. For the saturated turbulence driven in $f = 4; \epsilon = 0.8$, from Figure 6(V), the percentage of rotational energy injected into the fluid is $\overline{Ro_{eq}}^2/2 \sim 1\%$ generating strong turbulence where $\overline{Re_{eq}} = 6.25 \times 10^3$. For celestial bodies where $E \sim 10^{-14}$, only a small percentage of the tremendous amounts of spin-orbital rotational energy must be transmitted into the fluid layer to drive strongly turbulent motions. These turbulent flows can lead to energy dissipation[58] that effects the orbital evolution of these bodies[55] and may drive dynamo processes. Convectively driven planetary magnetic field generation suffers from tight budget constraints.[59,60] Such energetic limitations become more severe in smaller bodies.[61] However, our results suggest that mechanically-forced orbital systems can harvest significant amounts of spin-orbital energy to drive turbulent processes without the need for convection. Together with recent numerical findings showing that mechanically forced instabilities can drive dynamos in precessing spheres,[18] spheroids,[19] in longitudinally-librating systems,[20] and in tidal forced systems,[21] our results support the possibility that mechanical forcing leads to dynamo generation in smaller bodies, like the early Moon[62] and asteroids,[63,64] explaining data that do not presently fit into the standard model for convective dynamos.

ACKNOWLEDGMENTS

APPENDIX A: EXPERIMENTAL PARAMETERS

TABLE II. Physical and dimensionless parameter definitions and their range of values in the experiment.

Parameter	Definition	Experiment
a	Long axis along $\hat{\mathbf{x}}$	127 mm
b	Short axis along $\hat{\mathbf{y}}$	89 mm
c	Short axis along $\hat{\mathbf{z}}$	89 mm
$\Omega_0/2\pi$	Mean rotation frequency	0.5 Hz
$\omega_{lib}/2\pi$	Libration frequency	0.25 - 5.0 Hz ±0.1%
ν	Kinematic viscosity	10^{-6} m^{2}s^{-1}
E	Ekman number $\nu/(\Omega_0 a^2)$	2×10^{-5}
f	ω_{lib}/Ω_0	0.5 - 9.0
$\Delta\phi$	Angular displacement	0.5 - 2.5 rad
ϵ	$(\Delta\phi)f$	0.06 - 2.4
β	$\frac{a^2-b^2}{a^2+b^2}$	0.34
$\overline{c}$	$\frac{c}{\sqrt{(a^2+b^2)/2}}$	0.812

APPENDIX B: EXPERIMENTAL DATA

TABLE III. Mean velocity magnitude and variance for laminar and turbulent flows and zonal flow data from Figure 4(d).

f	ϵ	$\langle|\overline{U_\phi}|/r\rangle$	$\overline{\langle|U|\rangle} = \overline{Ro_{eq}}$	$\langle|U|\rangle_{var}$	Bulk Interior Flow
1.46	0.146	0.005	0.025	2.04×10^{-6}	Laminar
1.46	0.292	0.02	0.057	6.95×10^{-5}	Laminar
1.46	0.438	0.05	0.152	8.62×10^{-4}	Laminar
1.46	0.584	0.08	0.2459	8.86×10^{-4}	Laminar
1.46	0.73	0.15	0.1931	7.44×10^{-4}	Intermittent
1.46	0.876	—	0.1234	1.00×10^{-3}	Intermittent
1.46	1.022	0.3	0.2489	2.3×10^{-3}	Intermittent
1.5	1.05	—	0.1681	1.40×10^{-3}	Intermittent
1.6	1.12	—	0.299	2.6×10^{-3}	Intermittent
2.4	1.68	—	0.3305	3.05×10^{-4}	Saturated
4.0	0.8	—	0.125	1.88×10^{-4}	Saturated

TABLE IV. Experimental data from Figure 5 laminar and turbulent flows. Laminar, intermittent turbulence, and saturated turbulence are determined through side-view direct visualization.

f	ϵ	Bulk Interior Flows	f	ϵ	Bulk Interior Flows	f	ϵ	Bulk Interior Flows
1	0.7	Laminar	1.38	0.58	Laminar	2	1.2	Intermittent
1	0.8	Laminar	1.3	0.58	Laminar	2	0.6	Intermittent
1	0.9	Laminar	1.3	0.46	Laminar	2	1	Intermittent
1.2	0.84	Laminar	1.38	0.46	Laminar	3	0.3	Saturation
1.2	0.96	Laminar	1.46	0.46	Laminar	3.5	0.35	Saturation
1.2	1.08	Laminar	1.46	0.64	Laminar	4	0.4	Saturation
1.2	1.2	Laminar	1.42	0.73	Laminar	3.5	0.175	Saturation
1.46	0.876	Laminar	1.54	0.73	Laminar	4.2	0.84	Saturation
1.46	0.584	Laminar	1.44	0.73	Laminar	4.4	1.32	Saturation
1.46	0.438	Laminar	1.46	0.69	Laminar	0.5	1.25	Saturation
1.46	0.292	Laminar	1.54	0.69	Laminar	4	0.8	Saturation
1.46	0.146	Laminar	1.54	0.64	Laminar	3	0.6	Saturation

Table IV. (*Continued.*)

f	ϵ	Bulk Interior Flows	f	ϵ	Bulk Interior Flows	f	ϵ	Bulk Interior Flows
1.6	0.48	Laminar	1.48	0.73	Laminar	2.4	1.992	Saturation
1.6	0.32	Laminar	1.48	0.69	Laminar	2.4	2.4	Saturation
1.6	0.16	Laminar	1.34	0.876	Laminar	2.4	0.48	Saturation
2	0.4	Laminar	1.34	0.82	Laminar	2.4	1.2	Saturation
4	0.08	Laminar	1.38	0.82	Laminar	0.5	1.44	Saturation
3.5	0.07	Laminar	1.42	0.78	Laminar	0.5	1.1	Saturation
3	0.06	Laminar	1.6	0.48	Laminar	0.5	1	Saturation
3	0.15	Laminar	1.52	0.69	Laminar	0.5	0.9	Saturation
4.2	0.21	Laminar	1.52	0.64	Laminar	2	0.8	Intermittent
4.2	0.42	Laminar	1.56	0.64	Laminar	0.74	0.82	Saturation
4.4	0.88	Laminar	1.58	0.64	Laminar	0.74	0.9768	Saturation
4.4	0.44	Laminar	1.38	0.64	Laminar	1.5	1.05	Intermittent
4.4	0.22	Laminar	1.48	0.64	Laminar	1.46	0.73	Intermittent
4.6	0.23	Laminar	1.38	0.78	Laminar	2	1.2	Intermittent
5	0.25	Laminar	1.48	0.61	Laminar	1.5	0.73	Intermittent
5.5	0.275	Laminar	1.46	0.58	Laminar	1.38	0.876	Intermittent
6	0.3	Laminar	1.5	0.61	Laminar	1.5	0.64	Intermittent
6.6	0.33	Laminar	1.52	0.61	Laminar	1.5	0.69	Intermittent
7	0.35	Laminar	1.56	0.61	Laminar	1.46	0.876	Intermittent
8	0.4	Laminar	2.4	0.12	Laminar	1.5	0.82	Intermittent
9	0.45	Laminar	2.4	0.24	Laminar	1.42	0.876	Intermittent
5	0.5	Laminar	2.6	0.442	Saturation	1.5	0.876	Intermittent
6	0.6	Laminar	2.76	0.4692	Saturation	1.42	0.82	Intermittent
7	0.7	Laminar	3	0.51	Saturation	1.46	0.78	Intermittent
5	1	Laminar	3.5	0.595	Saturation	1.5	0.78	Intermittent
0.5	0.5	Laminar	4	0.68	Saturation	1.52	0.73	Intermittent
0.5	0.45	Laminar	1.46	1.022	Intermittent	1.5	0.73	Intermittent
0.5	0.4	Laminar	1.6	1.12	Intermittent	1.38	0.876	Intermittent
0.5	0.35	Laminar	2	1.4	Intermittent	1.5	0.64	Intermittent
2.4	0.12	Laminar	2.4	1.68	Saturation	1.5	0.69	Intermittent
2.4	0.24	Laminar	1.8	1.26	Intermittent	1.46	0.876	Intermittent
0.74	0.675	Laminar	1	1	Intermittent	1.5	0.82	Intermittent
1.38	0.73	Laminar	1.46	0.876	Intermittent	1.42	0.876	Intermittent
1.3	0.73	Laminar	1.6	0.96	Intermittent	1.5	0.876	Intermittent
1.26	0.73	Laminar	1.6	0.8	Intermittent	1.42	0.82	Intermittent
1.5	0.58	Laminar	1.6	0.64	Intermittent	...	...	...
2.4	0.12	Laminar	4	0.16	Intermittent	...	...	...
2.4	0.24	Laminar	1.46	0.73	Intermittent	...	...	...

[1] R. Comstock and B. Bills, "A solar system survey of forced librations in longitude," J. Geophys. Res. : Planets **108**, 1–13, doi: 10.1029/2003JE002100 (2003).

[2] J. Margot, S. Peale, R. Jurgens, M. Slade, and I. Holin, "Large longitude libration of Mercury reveals a molten core," Science **316**, 710–714 (2007).

[3] J. Anderson, W. Sjogren, and G. Schubert, "Galileo gravity results and the internal structure of Io," Science **272**, 709–712 (1996).

[4] G. Schubert, J. Anderson, T. Spohn, and W. Mckinnon, "Interior composition, structure, and dynamics of the Galilean satellites," in *Jupiter: The Planet, Satellites, and Magnetosphere* (Cambridge University, 2004).

[5] J. Anderson, G. Schubert, R. Jacobson, E. Lau, W. Moore, and W. Sjogren, "Europa's differentiated internal structure: Inference from four Galileo encounters," Science **281**, 2019–2022 (1998).

[6] J. Anderson, R. Jacobson, T. McElrath, W. Moore, G. Schubert, and P. Thomas, "Shape, mean radius, gravity field, and interior structure of Callisto," Icarus **153**, 157–161 (2001).

[7] J. Noir, F. Hemmerlin, J. Wicht, S. Baca, and J. M. Aurnou, "An experimental and numerical study of librationally driven flow in planetary cores and subsurface oceans," Phys. Earth Planet. Inter. **173**, 141–152 (2009).

[8] M. Calkins, J. Noir, J. Eldredge, and J. Aurnou, "Axisymmetric simulations of libration-driven fluid dynamics in a spherical shell geometry," Phys. Fluids **22**, 1–12 (2010).

[9] A. Sauret, D. Cébron, C. Morize, and M. Le Bars, "Experimental and numerical study of mean zonal flows generated by librations of a rotating spherical cavity," J. Fluid Mech. **662**, 260–268 (2010).

[10] J. Noir, D. Cébron, M. Le Bars, A. Sauret, and J. M. Aurnou, "Experimental study of libration-driven flows in non-axisymmetric containers," Phys. Earth Planet. Inter. **204-205**, 1–10 (2012).

[11] M. Calkins, J. Noir, J. Eldredge, and J. M. Aurnou, "The effects of boundary topography on convection in Earth's core," Geophys. J. Inter. **189**, 799–814 (2012).

[12] B. Deleplace and P. Cardin, "Viscomagnetic torque at the core mantle boundary," Geophys. J. Inter. **167**, 557–566 (2006).

[13] B. Buffett and U. Christensen, "Magnetic and viscous coupling at the core-mantle boundary: Inferences from observations of Earth's rotation," Geophys. J. Inter. **171**, 145–152 (2007).

[14] P. Roberts and J. M. Aurnou, "On the theory of core-mantle coupling," Geophys. Astrophys. Fluid Dyn. **106**, 157–230 (2012).

[15] A. Kagayama and T. Sato, "Computer simulation of a magnetohydrodynamic dynamo II," Phys. Plasmas **2**, 1421–1431 (1995).

[16] G. Glatzmeier and P. Roberts, "Rotation and magnetism of Earth's inner core," Science **274**, 1887–1891 (1996).

[17] G. Schubert and K. Soderlund, "Planetary magnetic fields: Observations and models," Phys. Earth Planet. Inter. **187**, 92–108 (2011).

[18] A. Tilgner, "Precession driven dynamos," Phys. Fluids **17**, 034104 (2005).

[19] C. Wu and P. Roberts, "On a dynamo driven by topographic precession," Geophys. Astrophys. Fluid Dyn. **13**, 467–501 (2009).

[20] C. Wu and P. Roberts, "On a dynamo driven topographically by longitudinal libration," Geophys. Astrophys. Fluid Dyn. **107**, 20–44 (2013).

[21] D. Cébron and R. Hollerbach, "Tidally driven dynamos in a rotating sphere," Astrophys. J., Lett. **789**, L25 (2014).

[22] K. Aldridge, "An experimental study of axisymmetric inertial oscillations of a rotating sphreical container," Ph.D. thesis (Massachusetts Institute of Technology, 1967).

[23] K. Aldridge and A. Toomre, "Axisymmetric inertial oscillation of a fluide in a rotating spherical container," J. Fluid Mech. **37**, 307–323 (1969).

[24] K. Zhang, K. Chan, X. Liao, and J. M. Aurnou, "The non-resonant response of fluid in a rapidly rotating sphere undergoing longitudinal libration," J. Fluid Mech. **720**, 212–235 (2013).

[25] C.-Y. Wang, "Cylindrical tank of fluid oscillating about a state of steady rotation," J. Fluid Mech. **41**, 581–592 (1970).

[26] A. Sauret and S. Le Dizes, "Libration-induced mean flow in a spherical shell," J. Fluid Mech. **718**, 181–209 (2013).

[27] K. Chan, X. Liao, and K. Zhang, "Simulations of fluid motions in ellipsoidal planetary cores driven by longitudinal libration," Phys. Earth Planet. Inter. **187**, 139–403 (2011).

[28] K. Zhang, K. Chan, and X. Liao, "On fluid motion in librating ellipsoids with moderate equatorial eccentricity," J. Fluid Mech. **673**, 468–479 (2011).

[29] R. Kerswell and W. Malkus, "Tidal instability as the source for Io's magnetic signature," Geophys. Res. Lett. **25**, 603–606, doi: 10.1029/98GL00237 (1998).

[30] D. Cébron, M. Le Bars, C. Moutou, and P. Le Gal, "Elliptical instability in terrestrial planets and moons," Astron. Astrophys. **539**, A78 (2012).

[31] W. V. R. Malkus, "An experimental study of global instabilities due to tidal(elliptical) distortion of a rotating eloastic cylinder," Geophys. Astrophys. Fluid Dyn. **48**, 123–134 (1989).

[32] D. Cébron, M. Le Bars, J. Noir, and J.M. Aurnou, "Libration driven elliptical instability," Phys. Fluids **24**, 061703 (2012).

[33] M. Le Bars, D. Cébron, and P. Le Gal, "Flows driven by libration, precession, and tides," Annu. Rev. Fluid Mech. **47**, 163–194 (2015).

[34] F. Busse, "Mean zonal flows generated by librations of a rotating spherical cavity," J. Fluid Mech. **650**, 505–512 (2010).

[35] F. Busse, "Zonal flow induced by longitudinal librations of a rotating cylindrical cavity," Phys. D **240**, 208–211 (2011).

[36] J. Noir, M. Calkins, M. Lasbleis, J. Cantwell, and J. M. Aurnou, "Experimental study of libration-driven zonal flows in a straight cylinder," Phys. Earth Planet. Inter. **182**, 98–1106 (2010).

[37] A. Sauret, D. Cébron, M. Le Bars, and S. Le Dizes, "Fluid flows in a librating cylinder," Phys. Fluids **24**, 1–23 (2012).

[38] A. Sauret, "Forçage harmonique d'Écoulements en rotation: Vents zonaux, ondes inertielles et instabilités," Ph.D. thesis (Universite Aix-Marseille, 2012).

[39] H. Greenspan, *The Theory of Rotating Fluids* (Cambridge University Press, 1969).

[40] A. Tilgner, "8.07 - rotational dynamics of the core," in *Treatise on Geophysics*, edited by G. Schubert (Elsevier, 2007), pp. 207–243.

[41] R. Kerswell, "Elliptical instabilities of stratified, hydromagnetic waves," Geophys. Astrophys. Fluid Dyn. **72**, 107–144 (1993).

[42] W. Herreman, "Instabilité ellitpiquesous champ magnétique et dynamo d'ondes inertielles," Ph.D. thesis (Aix-Marseille Université, 2009).

[43] K. Zhang, X. Liao, and P. Earnshaw, "On inertial and oscillations in a rapidly rotating spheroid," J. Fluid Mech. **504**, 1–40 (2004).

[44] S. Vantieghem, "Inertial modes in a rotating triaxial ellipsoid," Proc. R. Soc. A **470**, 20140093 (2014).

[45] M. Rieutord and L. Valdettaro, "Inertial waves in a rotating spherical shell," J. Fluid Mech. **341**, 77–99 (1997).

[46] M. Rieutord, B. Georgeot, and L. Valdettaro, "Inertial waves in a rotating spherical shell: Attractors and asymptotic spectrum," J. Fluid Mech. **435**, 103–144 (2001).

[47] D. Cébron, S. Vantieghem, and W. Herreman, "Libration driven multipolar instabilities," J. Fluid Mech. **739**, 502–543 (2014).

[48] E. Gledzer and V. Ponomarev, "Instability of bounded flows with elliptical streamlines," J. Fluid Mech. **240**, 1–30 (1992).

[49] S. Le Dizes, "Three-dimensional instability of a multipolar vortex in a rotating flow," Phys. Fluids **12**, 2762–2774 (2000).

[50] J. K. Kevorkian and J. D. Cole, *Multiple Scale and Singular Perturbation Methods*, Applied mathematical sciences (Springer New York, 1996), Vol. 114.

[51] P. Meunier and T. Lewecke, "Analysis and treatment of errors due to high velocity gradients in particle image velocimetry," Exp. Fluids **35**, 408–421 (2003).

[52] C. Morize, M. Le Bars, P. Le Gal, and A. Tilgner, "Experimental determination of zonal winds driven by tides," Phys. Rev. Lett. **104**, 214501 (2010).

[53] H. Bondi and R. Lyttleton, "On the dynamical theory of the rotation of the Earth. II. The effect of precession on the motion of the liquid core," Proc. Cambridge Philos. Soc. **49**, 498–515 (1953).

[54] A. Sauret, M. Le Bars, and P. Le Gal, "Tide-driven shear instability in planetary liquid cores," Geophys. Res. Lett. **41**, 6078–6083 (2014).

[55] M. Le Bars, L. Lacaze, S. Le Dizes, P. Le Gal, and M. Rieutord, "Tidal instability in stellar and planetary binary systems," Phys. Earth Planet. Inter. **178**, 48–55 (2010).

[56] R. Kerswell, "Tidal excitation of hydromagnetic waves and their damping in the Earth," J. Fluid Mech. **274**, 219–241 (1994).

[57] L. Lacaze, P. Le Gal, and S. Le Dizes, "Elliptical instability in a rotating spheroid," J. Fluid Mech. **505**, 1–22 (2004).

[58] M. Rieutord, "Evolution of rotation in binaries: Physical processes," in Stellar Rotation, Proceeding IAU Symposium, **215** 394–403 (2003).

[59] J. Verhoogen, "Thermal regime of the Earth's core," Phys. Earth Planet. Inter. **7**, 47–58 (1973).

[60] M. Pozzo, C. Davies, D. Gubbins, and D. Alfé, "Thermal and electrical conductivity of iron at Earth's core conditions," Nature **485**, 355–358 (2012).

[61] F. Nimmo, "Energetics of asteroid dynamos and the role of compositional convection," Geophys. Res. Lett. **36**, L10201, doi: 10.1029/98GL00237 (2009).

[62] M. Le Bars, M. A. Wieczorek, O. Karatekin, D. Cébron, and M. Laneuville, "An impact-driven dynamo for the early Moon," Nature **479**, 215–218 (2011).

[63] R. Fu, B. Weiss, D. Shuster, J. Gattacceca, T. Grove, C. Suavet, E. Lima, L. Li, and A. Kuan, "An ancient core dynamo in asteroid Vesta," Science **338**, 238–241 (2012).

[64] J. A. Tarduno, R. Cottrell, F. Nimmo, J. Hopkins, J. Voronov, A. Erickson, E. Blackman, E. Scott, and R. Mckinney, "Evidence for a dynamo in the main group pallasite parent body," Science **338**, 93–95 (2012).